1998

Determining geostrophic velocity shear profiles with inverted echo sounders

Yuguang He
University of Rhode Island

D. Randolph Watts
University of Rhode Island, randywatts@uri.edu

Karen L. Tracey
University of Rhode Island, krltracey@uri.edu

Citation/Publisher Attribution

He, Y., D. R. Watts, and K. L. Tracey (1998), Determining geostrophic velocity shear profiles with inverted echo sounders, *J. Geophys. Res.*, 103(C3), 5607–5622, doi: 10.1029/97JC03439.
Available at: https://doi.org/10.1029/97JC03439

JOURNAL OF GEOPHYSICAL RESEARCH, VOL. 103, NO. C3, PAGES 5607–5622, MARCH 15, 1998

Determining geostrophic velocity shear profiles with inverted echo sounders

Yuguang He, D. Randolph Watts, and Karen L. Tracey

Graduate School of Oceanography, University of Rhode Island, Narragansett

Abstract. It is known that vertical acoustic travel time (τ), round-trip from the seafloor to the sea surface as measured by inverted echo sounders (IESs), can be interpreted in terms of dynamic height. This relationship is generalized and quantified in this paper for dynamic height ($\Delta D_{i,j}$) integrated between a variety of pressure limits (p_i, p_j) which span different portions of the main thermocline. The generalized form of the $\Delta D_{i,j}(\tau)$ relationships is nonlinear; the conventional linear relationship is valid when the limits of integration span the entire main thermocline. Velocity and temperature records are shown to be highly correlated vertically, indicating that the variability of the Gulf Stream and adjacent eddy field is dominated by the lowest baroclinic mode, which is called a gravest empirical mode (GEM). A "parallel isotherms model" is used to approximate the GEM and to develop analytic expressions for the observed $\Delta D_{i,j}(\tau)$ relationships in the Gulf Stream. The analytic expressions represent the observations well, with noise-to-signal variance ratios that are typically 1%. Using these new $\Delta D_{i,j}(\tau)$ relationships, the baroclinic velocity structure can be determined geostrophically by measuring the horizontal gradients with laterally separated τ measurements from IESs. Baroclinic velocities determined from a two-dimensional array of IESs in the Gulf Stream during 1988–1990 agree with velocity shears directly measured by current meters. The rms velocity difference between these two measurements of velocity shear at 400 dbar relative to 1000 dbar was 12 cm s^{-1} in the presence of typical currents of 50 cm s^{-1}. Ageostrophic motions (at both mesoscale and submesoscale), measured by the current meters but not by the IESs, contribute most of the velocity differences.

1. Introduction

The inverted echo sounder (IES) is a bottom moored instrument that measures the time (τ) required for an acoustic ping to travel to the sea surface and back [*Chaplin and Watts*, 1984]. Because the speed at which sound travels through water depends primarily on temperature, τ depends on the thermal structure of the water column through which the sound passes.

Rossby [1969] found that a linear relationship exists between τ and the depth of the main thermocline. *Watts and Rossby* [1977] extended the physical interpretation of the IES measurement by working with a linear relationship between τ and the dynamic height anomaly ΔD. Other researchers have verified the linearity of the $\Delta D(\tau)$ relationship in other oceanic regions such as in the eastern equatorial Pacific [*Miller et al.*, 1985; *Chiswell et al.*, 1987, 1988], central equatorial Pacific [*Chiswell et al.*, 1986; *Wimbush et al.*, 1990], South Atlantic [*Katz*, 1987; *Garzoli and Garraffo*, 1989; *Garzoli and Gordon*, 1996], and areas from the northern Sargasso Sea to Ireland [*Trivers and Wimbush*, 1994]. The scatter about a straight line is generally low when the T–S relationship is reasonably tight within the main thermocline, although *Hallock* [1987] notes that slightly better fits can be obtained if quadratic regressions are used instead.

Kim and Watts [1994] employed a linear $\Delta D(\tau)$ relationship to determine baroclinic velocities at 400 m in the Gulf Stream using IESs. Contoured maps of the IES-measured ΔD were treated as baroclinic geostrophic stream functions, the two-dimensional gradients of which were differentiated to yield vector velocity estimates. Velocities calculated in this manner were found to agree well with the directly measured current shear.

In these previous studies the dynamic height was treated as linearly related to τ. We show in section 2 that this linear relationship holds approximately when the dynamic height integral spans the strongly baroclinic structure such that the upper and lower levels p_i and p_j are above and below the main thermocline.

In the present study the functional relationship of dynamic height $\Delta D_{i,j}$ to τ is investigated between a variety of pressure intervals (p_i, p_j). The single measurement of τ is shown to provide an estimate of $\Delta D_{i,j}$ between a variety of intervals (albeit not independent). It is shown that the general relationship $\Delta D_{i,j}(\tau)$ is curved when the interval (p_i, p_j) is more restricted than the range through which the main thermocline shifts vertically. These $\Delta D_{i,j}(\tau)$ relationships are

Paper number 97JC03439.
0148-0227/98/97JC-03439$09.00

used to determine the baroclinic velocity ($V_{i,j}$) structure of the Gulf Stream, and the derived currents are shown to agree well with direct measurements.

Density, $\Delta D_{i,j}$, and velocity shear are all related between various pressure levels because the ocean mesoscale to large-scale variability is dominated by a gravest empirical mode structure. Section 4 quantifies the vertical correlations of the velocity and temperature variability observed independently by current meters. The variability is shown to be represented approximately by a parallel isotherms model, providing a methodology to estimate both the signal and the uncertainty of the dynamic height and velocity fields obtained from inverted echo sounders. This gravest mode dominance greatly simplifies the interpretation one may make of the whole mesoscale structure of the Gulf Stream and is the foundation on which rests the ability to obtain the vertical structure of the variability not only from IESs but also from other measurement techniques, such as the sea level measurements of altimeters.

2. $\Delta D_{i,j}(\tau)$ in the Gulf Stream

Both dynamic height and travel time are integral quantities which depend on the density ρ and sound speed c profiles. Because ρ and c usually depend mainly on temperature, ΔD and τ are intrinsically related. The integral form of the vertical round-trip travel time through the full water column is

$$\tau = 2\int_B^\eta c^{-1}dz = -2\int_{p_B}^0 \rho^{-1}g^{-1}c^{-1}dp \qquad (1)$$

where g is gravity and the integration ranges from the bottom B, where $p = p_B$, to the surface η, where $p = 0$.

The dynamic height anomaly is

$$\Delta D_{i,j} = \int_{p_i}^{p_j} \delta dp \qquad (2)$$

where p_i and p_j represent any two pressures and $\delta = \delta(S, T, p)$ is the specific volume anomaly. We include subscripts on $\Delta D_{i,j}$ to emphasize the dependence on the integration limits. When $p_j = p_B$ and $p_i = 0$, $\Delta D_{i,j}$ is a linear function of τ whose slope is determined by the stratification and T-S properties which characterize the geographic region [cf. *Hallock*, 1987; *Trivers and Wimbush*, 1994].

Now we investigate a more general case, allowing the two levels (p_i, p_j) to span only a portion of the water column. We will find that the dynamic height anomaly can still be expressed as a function of travel time, $\Delta D_{i,j} = \Delta D_{i,j}(\tau)$, but the relationship is not linear.

2.1. Data Analysis

The quantities τ and $\Delta D_{i,j}$ were calculated from historical hydrographic data in the Gulf Stream region according to (1) and (2). Nearly 400 hydrostations were used from the region 34°N to 41°N and 60°W to 75°W (Figure 1), all extending to at least 3500 dbar with sufficient vertical resolution for the above integrations. The hydrographic data were obtained from three sources: 107 conductivity-temperature-depth (CTD) and salinity-temperature-depth (STD) stations from the National Oceanographic Data Center (NODC),

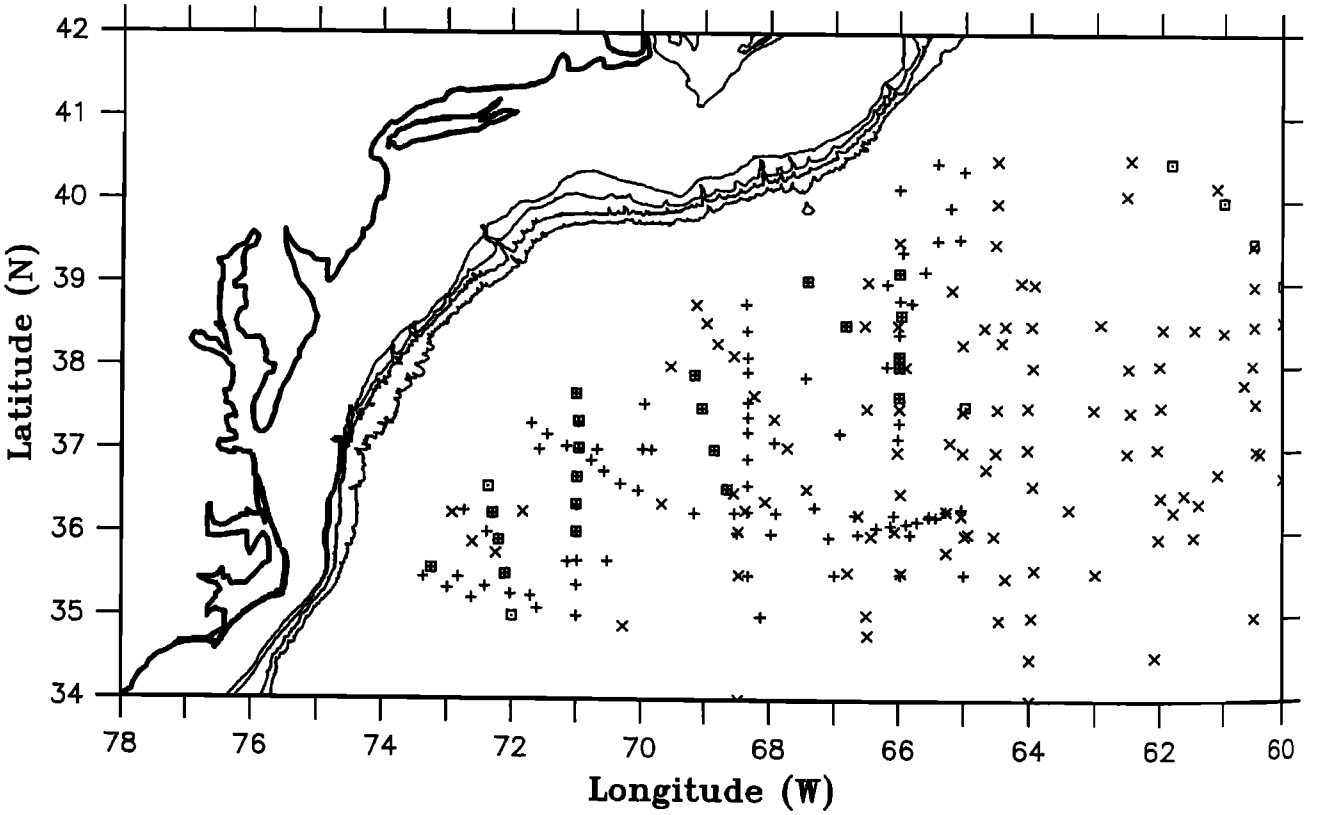

Figure 1. Locations of the hydrographic stations obtained from NODC (pluses), WHOI (squares), and M. McCartney (crosses). The bathymetric contours indicate the depths 100, 200, 1000, and 2000 m.

35 CTD stations from the Woods Hole Oceanographic Institution (WHOI), and 250 bottle stations from a quality-controlled historical assemblage provided to us by M. McCartney.

In calculating the τ integrals up to the sea surface the uppermost temperature and salinity measurements, typically at ~10 dbar depth, were assumed to be within the mixed layer and were treated as if they extended to the surface. The lower integration limit for τ was chosen to be 3500 dbar. However, the results presented in this paper were only weakly affected by the choice of p_B as long as $p_B > 2000$ dbar because the variability of τ and $\Delta D_{i,j}$ in the deep water was relatively small. For example, *Hallock* [1987] reports that negligible differences in the slope of the $\Delta D(\tau)$ relationship were obtained when the lower limit was chosen to be either 3000 or 5000 dbar.

The dynamic height anomaly $\Delta D_{i,j}$ was calculated over a variety of integration limits. The upper limit p_i was always 100 dbar or deeper in order to reduce variability associated with the seasonal pycnocline.

2.2. Systematic Variation of $\Delta D_{i,j}$ With τ

The calculated $\Delta D_{i,j}$ for several (p_i, p_j) choices are plotted as functions of τ in Figure 2. In Figures 2a, 2b, and 2c the data are grouped according to the varying pressure limits. In each plot the abscissa τ has the same range, 4.57–4.61 s (with shorter τ corresponding to deeper thermocline depths, generally occurring offshore). Figure 2a shows $\Delta D_{i,j}$ for three cases in which the deeper integration limit varies (3500, 2000, and 700 dbar) and the shallow limit is fixed (100 dbar). Cases where the deep integration limit is held constant (2000 dbar) and the shallow limit shifts deeper (200, 400, and 700 dbar) are shown in Figure 2b. The combined effects of varying both pressure levels are shown in Figure 2c. There is a substantial decrease in $\Delta D_{i,j}$, and the relationships become progressively more curved when the (p_i, p_j) range is decreased.

The observed changes in the slope $d[\Delta D_{i,j}(\tau)]/d\tau$ as a function of τ, p_i, and p_j can be understood by examining Figure 3, which shows a typical Gulf Stream temperature section, with one midthermocline isotherm (12°C) emphasized by the bold curve. The thermocline Z_T slopes downward across the Gulf Stream, so that the temperature of the Slope Water to the north is colder than that of the Sargasso Sea to the south at the same depth.

In Figure 3c the corresponding τ decreases by more than 0.03 s as Z_T deepens by 675 m across the Gulf Stream. Figure 3b shows the profile of $\Delta D_{0,3500}$ across this same Gulf Stream transect; $\Delta D_{0,3500}$ is ~1 dynamic meter (dyn. m) larger on the offshore (deep thermocline) side of the current.

The fact that the shapes of the τ and $\Delta D_{0,3500}$ profiles in Figure 3 mimic that of the thermocline gives rise to the linear relationships between the three quantities. Curvature occurs when the integration limits are narrowed such that part of the thermocline is excluded from the $\Delta D_{i,j}$ calculation: If the upper limit p_i is lowered, the thermocline will not be spanned completely on the shoreward side of the Gulf Stream. Consequently, the calculated $\Delta D_{i,j}$ will be less than those for the full integral, while τ continues to increase by the same amount. This leads to the observed flattening in the slope $d[\Delta D_{i,j}(\tau)]/d\tau$ for long τ (Figure 2b). Likewise, when the lower limit p_j is raised, a portion of the thermocline will be excluded from the $\Delta D_{i,j}$ integration on the offshore side. This leads to the observed flattening in the slope at short τ (Figure 2a).

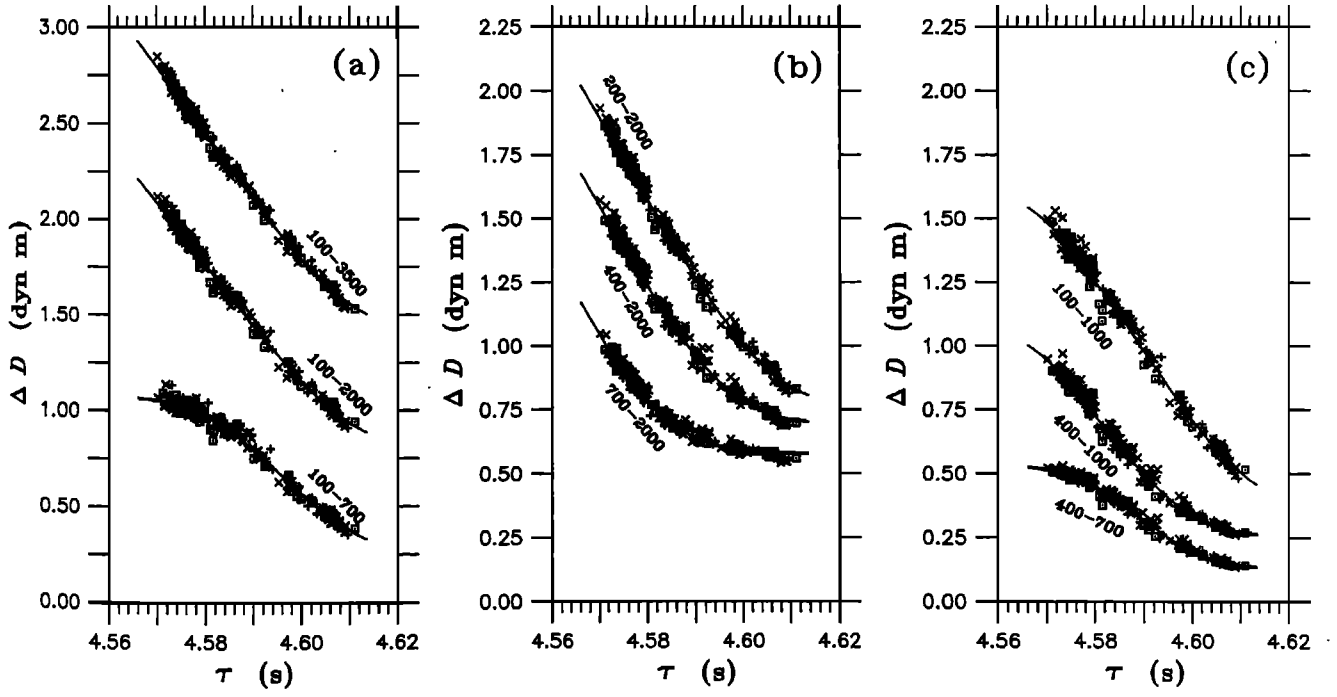

Figure 2. $\Delta D_{i,j}$ as functions of τ in the Gulf Stream. $\Delta D_{i,j}$ are grouped according to which pressure limit was varied: (a) lower limit p_j is varied, while upper limit is fixed at $p_i = 100$ dbar, (b) upper limit p_i is varied, while $p_j = 2000$ dbar, and (c) both p_i and p_j are varied. The modeled curves are superimposed.

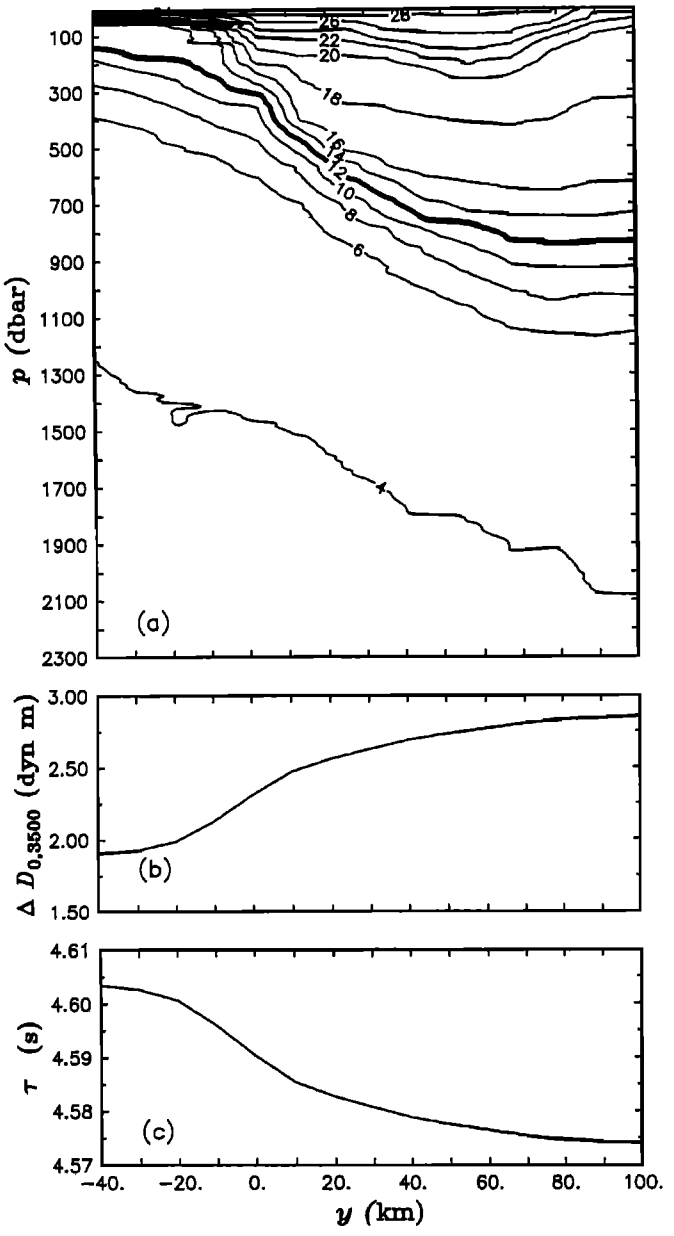

Figure 3. Cross-stream sections of (a) temperature T, (b) $\Delta D_{0,3500}$, and (c) τ determined from hydrographic measurements taken across the Gulf Stream in July 1982.

2.3. Parallel Isotherms Model

In this section we seek an analytic expression which can represent the whole set of empirical $\Delta D_{i,j}(\tau)$ relationships shown in Figure 2. This process is facilitated by representing the temperature and δ structure as a smoothed function; using a smoothed integrand enforces a degree of consistency between integration results using different limits. The approximation employed here is that the isotherms in Figure 3a are nearly parallel as they deepen across the current. This behavior is also evident in Figures 4a and 4b, in which numerous T and δ profiles from casts that span the Gulf Stream are superimposed. The curves exhibit a similar shape through the thermocline (pycnocline) region. As shown in Figures 4c and 4d, shifting these δ and T profiles to align their main thermocline depths collapses all but the waters warmer than 18°C onto a single trace. The agreement is improved further when the top 100 dbar of the water column are excluded (Figures 4e and 4f).

Therefore it seemed appropriate to employ the following "parallel isotherms model" to represent the cross-stream structure. The δ profile of Figure 4f can be represented by a hyperbolic tangent function of the form

$$\delta = B_1 - B_2 \tanh[(p - p_t - \mu_2)\mu_1] \tag{3}$$

The main thermocline depth p_t was determined from the τ measurements as $p_t = M\tau + B_{\text{INT}}$ with $M = -21345\ \text{m s}^{-1}$ and $B_{\text{INT}} = 98475$ m.

By integrating δ according to (2), $\Delta D_{i,j}$ is obtained as

$$\Delta D_{i,j} = B_1(p_j - p_i) - \frac{B_2}{\mu_1} \ln\left\{\frac{\cosh[(p_j - p_t - \mu_2)\mu_1]}{\cosh[(p_i - p_t - \mu_2)\mu_1]}\right\} \tag{4}$$

where B_1 and μ_2 are offsets of the linear and nonlinear parts of the function, respectively. B_2 and μ_1 are the linear and nonlinear scale factors, respectively.

The four coefficients were determined by least squares regression on the $\Delta D_{i,j}$ observations shown in Figure 2 for each (p_i, p_j) interval. This was a two-step process: To determine the nonlinear coefficients, a grid of trial values (μ_1, μ_2) was generated, and for each (μ_1, μ_2) pair a preliminary set of linear coefficients was found by selecting the (B_1, B_2) values which minimized the root-mean-square (rms) difference between the fitted curve and the observations. The optimal (μ_1, μ_2) combination for each (p_i, p_j) interval was chosen from the set of trial values by selecting the pair for which the smallest rms difference overall was obtained. A single pair of (μ_1, μ_2) coefficients was found to be adequate to produce the close-to-minimum rms value for all the $\Delta D_{i,j}(\tau)$; these coefficients were $\mu_1 = 0.003461\ \text{dbar}^{-1}$ and $\mu_2 = 26.24$ dbar.

Using these constant values of (μ_1, μ_2), the optimal linear coefficients (B_1, B_2) for each (p_i, p_j) were determined using least squares regression. Table 1 lists the coefficients (B_1, B_2) for the suite of pressure intervals investigated. The coefficients vary by only ~5–7%. Although we used depth-interval-dependent (B_1, B_2) coefficients in this study, for many purposes it would be adequate to use a single pair. The final curves of this parallel isotherms model are superimposed on the observations in Figure 2.

2.4. Quantifying the Scatter of $\Delta D_{i,j}(\tau)$

Figure 2 shows that the $\Delta D_{i,j}$ relationship remains tight and exhibits approximately the same amount of scatter regardless of the integration limits, even for a drastically reduced integration range like 400–700 dbar. Figure 5a confirms that the standard deviation about essentially all of the curves was 2–2.5 dyn. cm. The highest values, obtained for $p_i = 100$ dbar, are associated with the variability of the seasonal thermocline. However, because the range of $\Delta D_{i,j}$ decreases as the range of integration decreases, it is important to verify that the amount of scatter for any desired (p_i, p_j) in-

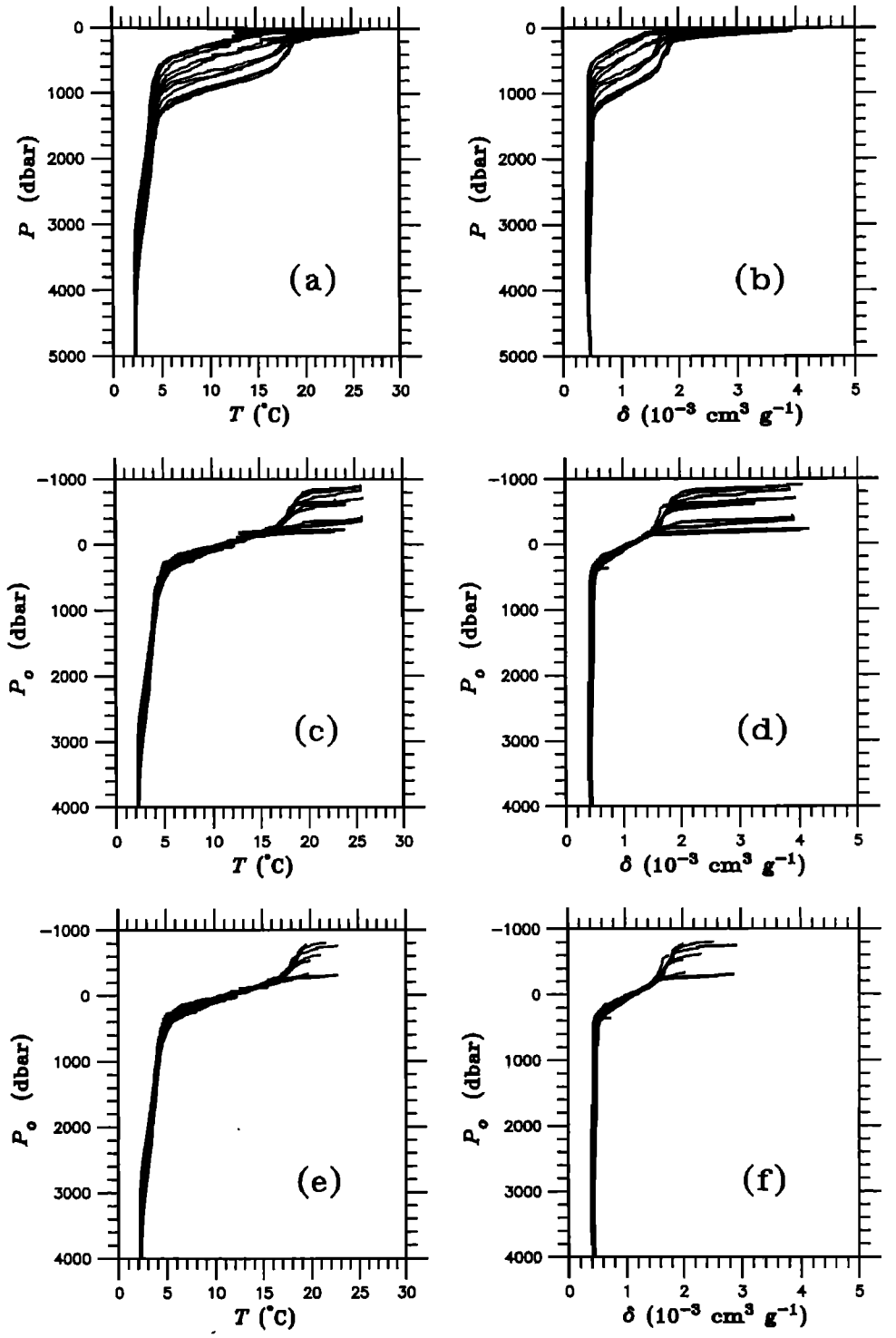

Figure 4. Temperature T and specific volume anomaly δ profiles across the Gulf Stream. (a) T versus p, (b) δ versus p, (c) vertically shifted T profile such that pressure of 12°C isotherm becomes the origin, (d) δ shifted same as 4c, (e) same as 4c except the upper 100 dbar of each T trace was removed, (f) same as 4e except for δ.

terval is significantly less than the $\Delta D_{i,j}$ signal. For this discussion the statistical property noise-to-signal ratio (NSR) is introduced.

Since the model curves fit the data well, they are treated as the true "signal." For each measured τ the corresponding $\Delta D_{i,j}$ signal can be calculated using the model. The variance of the signal is defined as the variance of these modeled $\Delta D_{i,j}$ values. By defining "noise" as the scatter about the signal the scatter can be determined by subtracting the modeled $\Delta D_{i,j}$ values from the observations. Potentially, the noise could be overestimated by this method if the curves do not fit the observations well. However, this does not appear

Table 1. Optimal Linear Coefficients Used to Determine $\Delta D_{i,j}(\tau)$for the Gulf Stream According to Equation (4) When $\mu_1 = 0.003461$ dbar^{-1} and $\mu_2 = 26.24$ dbar

Integration Limits, dbar	B_1, dyn. m dbar^{-1}	B_2, dyn. m dbar^{-1}	B_2/μ_1, dyn. m
700–3500	0.001434	0.001001	0.289216
700–2000	0.001293	0.000851	0.245889
700–1000	0.001191	0.000756	0.218503
400–3500	0.001275	0.000852	0.246239
400–2000	0.001205	0.000777	0.224479
400–1000	0.001140	0.000726	0.209909
400–700	0.001107	0.000704	0.203280
200–3500	0.001234	0.000820	0.236946
200–2000	0.001176	0.000760	0.219487
200–1000	0.001119	0.000718	0.207580
200–700	0.001094	0.000698	0.201651
100–3500	0.001229	0.000819	0.236590
100–2000	0.001175	0.000762	0.220166
100–1000	0.001124	0.000724	0.209171
100–700	0.001104	0.000709	0.204749
Mean	0.001194	0.000790	0.223641
±95% confidence limit	±0.000057	±0.000050	±0.015073

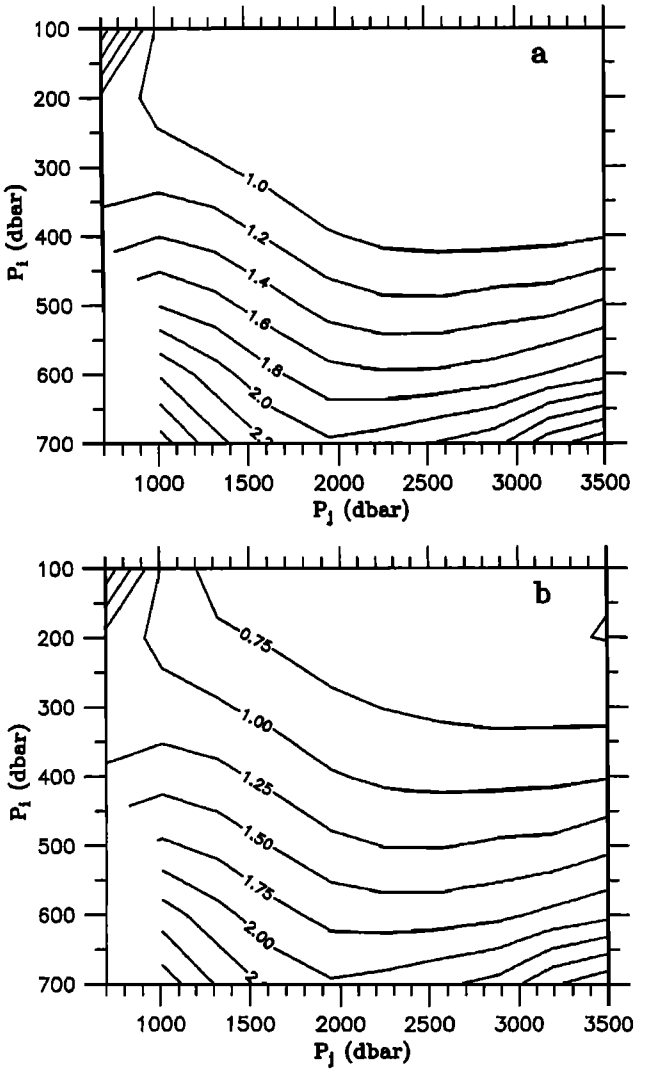

Figure 5. (a) Standard deviations and (b) noise-to-signal ratios (NSRs) for the Gulf Stream contoured as functions of upper and lower pressure (p_i, p_j) limits. Contours are dynamic centimeters for standard deviation and percent for NSR.

to be the case for the integration ranges shown in Figure 2. Table 2 lists the variances of both the $\Delta D_{i,j}$ signal and the noise for all pairs of pressure levels examined.

The corresponding NSRs, calculated as the ratios of these variances, are also listed in Table 2. In general, the NSRs are near 1%; however, they vary between a minimum 0.49% for the (200, 3500 dbar) integration limits and a maximum 2.95% for the (700, 3500 dbar) limits. The largest NSRs occur when upper integration limits are deep (~700 dbar), and lowest values occur when $\Delta D_{i,j}$ is integrated over the full thermocline region ($p_j \geq 2000$ dbar and $p_i \leq 200$ dbar). Figure 5b is a visual representation of Table 2. Figure 5b shows a large region of NSR $\leq$ 1% with the NSR values

Table 2. The Noise Variances, Signal Variances and Their Ratios Obtained for the Curves Shown in Figure 2 for the Suite of Integration Limits Indicated for the Gulf Stream

Integration limits, dbar	Noise Variance, (dyn. m)^2	ΔD Variance, (dyn. m)^2	NSR, %
700–3500	0.000774	0.026245	2.95
700–2000	0.000385	0.018956	2.03
700–1000	0.000219	0.007548	2.91
400–3500	0.000716	0.072792	0.98
400–2000	0.000607	0.060471	1.00
400–1000	0.000536	0.038365	1.40
400–700	0.000153	0.011851	1.29
200–3500	0.000554	0.112734	0.49
200–2000	0.000608	0.096704	0.62
200–1000	0.000637	0.067810	0.94
200–700	0.000343	0.029857	1.15
100–3500	0.000689	0.132788	0.52
100–2000	0.000770	0.114959	0.67
100–1000	0.000829	0.083040	1.00
100–700	0.000782	0.040268	1.94

NSR, noise-to-signal ratio.

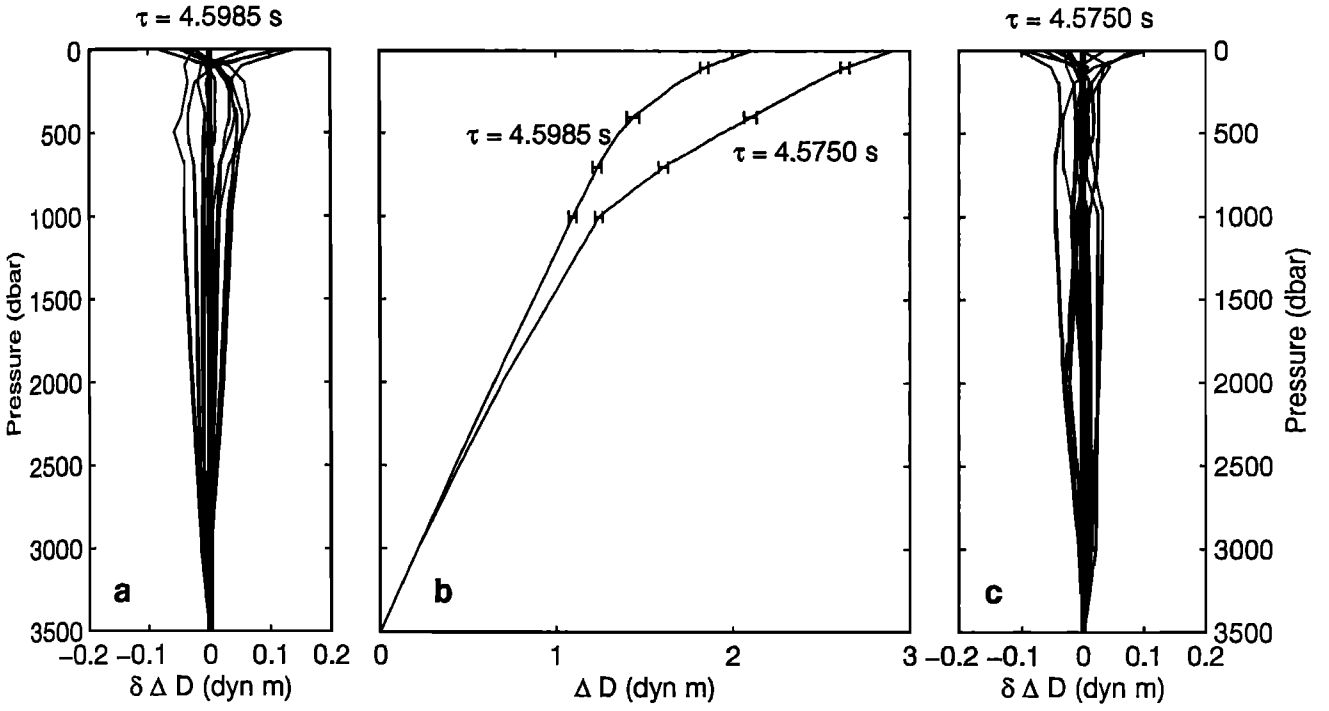

Figure 6. (a) and (c) Individual profiles of the differences between the model and measured ΔD are illustrated for 10 hydrocasts in each regime. (b) Vertical profiles of ΔD determined using the parallel isotherms model for two sets of hydrocasts, centered around $\tau_{3500} = 4.5985$ and 4.5750 s, respectively, which characterize the variability on the cold and warm sides of the Gulf Stream. Standard deviations between the measured and modeled ΔD profiles are indicated for the 100, 400, 700, and 1000 dbar levels.

increasing as the upper limit deepens. Although the NSRs obtained for $p_i = 100$ dbar are quite similar to those for $p_i = 200$ dbar, they are systematically higher. This increase is apparently caused by additional variability within the seasonal thermocline.

A comparison of the model-generated vertical profiles of $\Delta D_{i,j}$ with those obtained from the hydrographic measurements provides another means to assess the accuracy of the model. Since it is well known that several different vertical structures of ΔD can produce identical values of τ, such a test provides an estimate of the errors associated with the parallel isotherms assumption.

For this comparison we focused on two regimes across the Gulf Stream front: The first regime, defined by $\tau = 4.5985$ s, corresponded to the steeply sloping portion of the thermocline ($Z_{12} \approx 320$ dbar in Figure 3), and the second regime, defined by $\tau = 4.5750$ s, represented the offshore side of the Gulf Stream (with $Z_{12} \approx 830$ dbar). These choices of τ were used in (4) to produce the two vertical profiles of ΔD shown in Figure 6b.

Hydrocasts were grouped into the two regimes by selecting the casts whose τ were within ± 0.001 s of the specified values. In all, 11 casts were in the first regime, and 26 casts were in the second regime. For each cast, dynamic height profiles were determined from the measurements using (2) and from the model by using the corresponding τ in (4). The differences ($\delta\Delta D$) between the measured and the model profiles were determined. The standard deviations of these differences were calculated for the two regimes and are superimposed on the curves in Figure 6b. The standard deviations varied with the ΔD integration limits and regime, ranging from 0.4 to 3.7 dyn. cm for the 100 dbar level and below.

Figures 6a and 6c show 10 randomly chosen $\delta\Delta D$ profiles from each regime. In both regimes the curves appear to be evenly distributed about zero at all depths with the largest differences (~10 dyn. cm) confined to the upper 100 dbar, where seasonal variations are the greatest. The small deviations and the absence of bias at any level provide additional assurance that the model produces accurate vertical profiles of $\Delta D_{i,j}$ from IES τ measurements.

3. Baroclinic Velocities From $\Delta D_{i,j}(\tau)$

3.1. Gravest Empirical Mode (GEM) Methodology

Horizontal gradients of $\Delta D_{i,j}$ between adjacent sites can be used to determine the geostrophic baroclinic velocities normal to the measured gradients by

$$\mathbf{V}_{i,j} = \mathbf{V}_i - \mathbf{V}_j = f_0^{-1} \cdot \mathbf{k} \times \nabla(\Delta D_{i,j}) \qquad (5)$$

where $\mathbf{k}$ is the vertical unit vector, (i, j) denote two pressure levels, and f_0 is the Coriolis parameter. From the previously described $\Delta D_{i,j}(\tau)$ relationships, changes in ΔD can be determined from changes in τ by

$$d\Delta D_{i,j} = \frac{d[\Delta D_{i,j}(\tau)]}{d\tau} d\tau \qquad (6)$$

and baroclinic velocity can be expressed in terms of τ as

$$\mathbf{V}_{i,j} = f_0^{-1} \frac{d[\Delta D_{i,j}(\tau)]}{d\tau} \cdot \mathbf{k} \times \nabla\tau \qquad (7)$$

Since $\Delta D_{i,j}$ can be determined between any pair of pressure levels from the same measurement of τ, the vertical profile of velocity shear $\mathbf{V}_{i,j}$ may be estimated from the measurements of laterally separated IESs. Additionally, with a gridded array of IESs, τ gradients can be obtained in two directions to produce estimates of both velocity components.

Figure 7 is a cartoon which illustrates how vertical shear profiles are generated from the suite of functional relationships between $\Delta D_{i,j}$ and τ. The familiar relationship between geostrophic velocity and density is presented in Figure 7a, in which the horizontal distance along the x axis is indicated by "station number" or "site." Figure 7a shows that the depth of the strongest velocity shear varies in accord with the depth of the pycnocline. For example, between sites 2 and 3 where the pycnocline is shallow the largest shear in the velocity profile v_{3-2} is also shallow. On the other hand, between sites 5 and 6 both the pycnocline and the strongest shear in the v_{6-5} profile are deep. These two velocity profiles are superimposed (Figure 7b) with four points labeled (points a, b, c, and d) to emphasize their differences: Whereas at 100 dbar both the v_{3-2} and v_{6-5} velocities are strong (points a and c), at 700 dbar the v_{6-5} velocity (point d) is stronger than that of v_{3-2} (point b).

To illustrate how these two very different profiles can be obtained from IES measurements of τ, imagine one pair of IESs moored under a front similar to that shown in Figure 7. Imagine further that the front shifts laterally over the sites, so that the IESs will be under the shallow pycnocline (like sites 2 and 3) some of the time, while at other times the IESs will be under the deep pycnocline (like sites 5 and 6). When the pycnocline is shallow, the travel times measured by the IESs are longer than when the pycnocline is deep. Figure 7c depicts the τ measured at sites 2 and 3 by the right and left edges of the densely shaded bar, respectively, and the τ measured at sites 5 and 6 by the right and left edges of the lighter bar. The $\Delta D_{100,3500}(\tau)$ and $\Delta D_{700,3500}(\tau)$ curves of Figure 2 are repeated in Figure 7c.

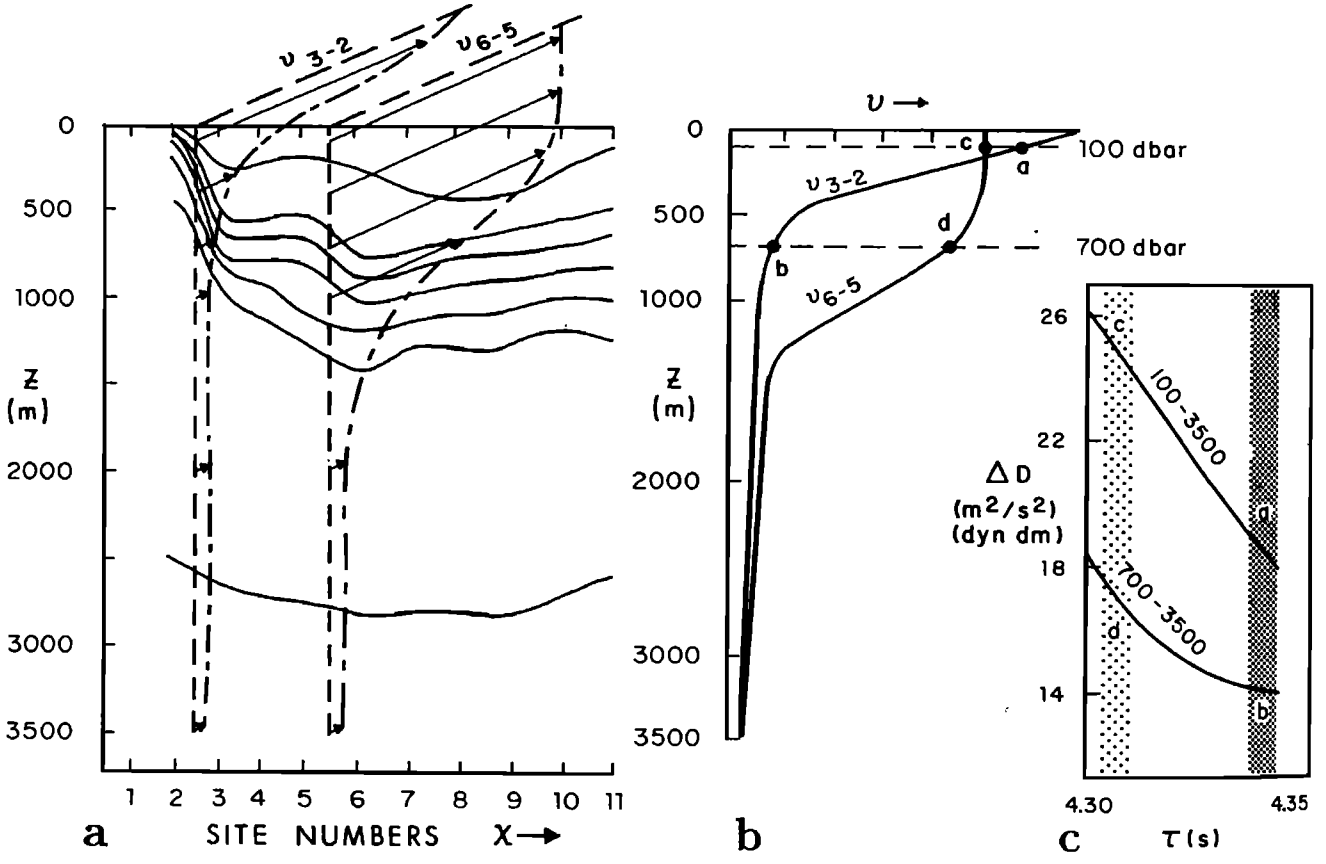

Figure 7. Schematic diagram showing how the velocity $\mathbf{V}_{IES}$ profiles are determined from the IES-measured τ. (a) Idealized vertical section of the pycnocline, where the cross-stream horizontal distance is indicated by "station number" or site. Vertical profiles of horizontal velocity are sketched for two locations: v_{3-2} is average between sites 2 and 3, and v_{6-5} is average between sites 5 and 6. (b) Superimposition of two velocity profiles. The v_{3-2} velocities at 100 and 700 dbar are indicated by points a and b, respectively. The v_{6-5} velocities at the same depths are indicated by points c and d. (c) $\Delta D_{100,3500}$ and $\Delta D_{700,3500}$ are shown as functions of τ. The densely shaded bar spans the two τ measured at sites 2 and 3, and the lighter bar spans the two τ measured at sites 5 and 6. The $\Delta D_{i,j}$ gradients labeled points a, b, c, and d correspond to the respectively labeled velocities in Figure 7b.

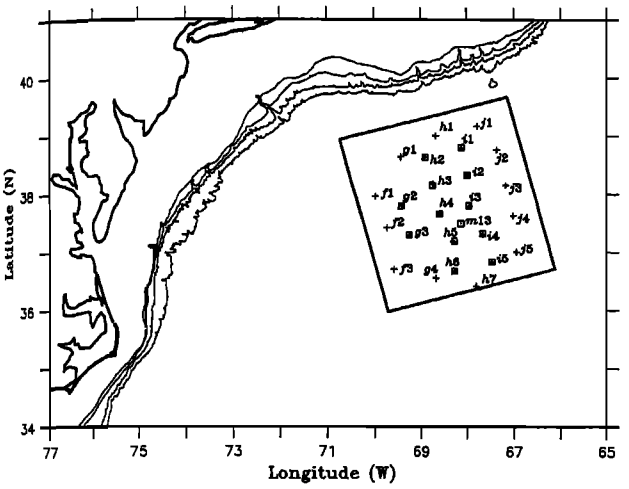

Figure 8. Synopoptic Ocean Prediction (SYNOP) Central Array. IES locations are indicated by the crosses and current meters are indicated by the squares. Site designations are labeled. Bathymetric contours are the same as in Figure 1.

Focusing first on the $\Delta D_{100,3500}(\tau)$ curve, a large dynamic height gradient is obtained between sites 2 and 3 (point a, Figure 7c). Using this gradient in (5) yields the large v_{3-2} velocity labeled as point a in Figure 7b. At sites 5 and 6 the τ values, while both smaller than at sites 2 and 3, differ such that the $\Delta D_{100,3500}$ gradient (point c, Figure 7c) is of comparable size, and the resulting velocity (point c, Figure 7b) is again large.

Next, focus on the $\Delta D_{700,3500}(\tau)$ relationship and the 700 m velocities. Between sites 5 and 6, with the same τ difference as noted above, the $\Delta D_{700,3500}$ gradient (point d, Figure 7c) is nearly equal to the $\Delta D_{100,3500}$ gradient (point c), and the velocities at 100 and 700 m (points c and d) are correspondingly of similar size. By contrast, between sites 2 and 3 the $\Delta D_{700,3500}$ gradient (point b, Figure 7c) is much smaller than the $\Delta D_{100,3500}$ gradient (point a) because the slope of the $\Delta D_{700,3500}(\tau)$ curve is flattened; correspondingly, the velocity at point b is considerably weaker. Restating this GEM result more generally, the curvature of the $\Delta D_{i,j}(\tau)$ relationship changes the slope $d[\Delta D_{i,j}(\tau)]/d\tau$ in (7) to produce realistic lateral and vertical structures of the velocity field.

Sections 3.2–3.4 examine how well the velocity structure in the Gulf Stream can be determined by IESs using these relationships. Geostrophic velocities $\mathbf{V}_{\text{IES}}$ at several levels were calculated from actual IES τ measurements. These are compared with independently measured shear currents $\mathbf{V}_{\text{CM}}$ to evaluate the technique.

3.2. Data Sources

As a part of the Synoptic Ocean Prediction (SYNOP) experiment, 24 IESs were deployed in an array spanning the Gulf Stream. The array (Figure 8) was centered near 38°N, 68°W and was in place from June 1988 to August 1990.

The IES τ measurements were converted to dynamic height anomaly using (4). Gridded fields of $\Delta D_{i,j}$ were produced for the boxed region in Figure 8 using optimal interpolation (OI) [*Tracey et al.*, 1997]. Examples of the $\Delta D_{400,1000}$ maps are shown in Figure 9a. The maps show a large-amplitude meander trough in the array which evolved and propagated during that 15-day period.

In addition to the IESs, 13 current meter moorings (CMs) were deployed in the array. Each mooring had current meters at four depths (3500, 1000, 700, and 400 m), reaching from

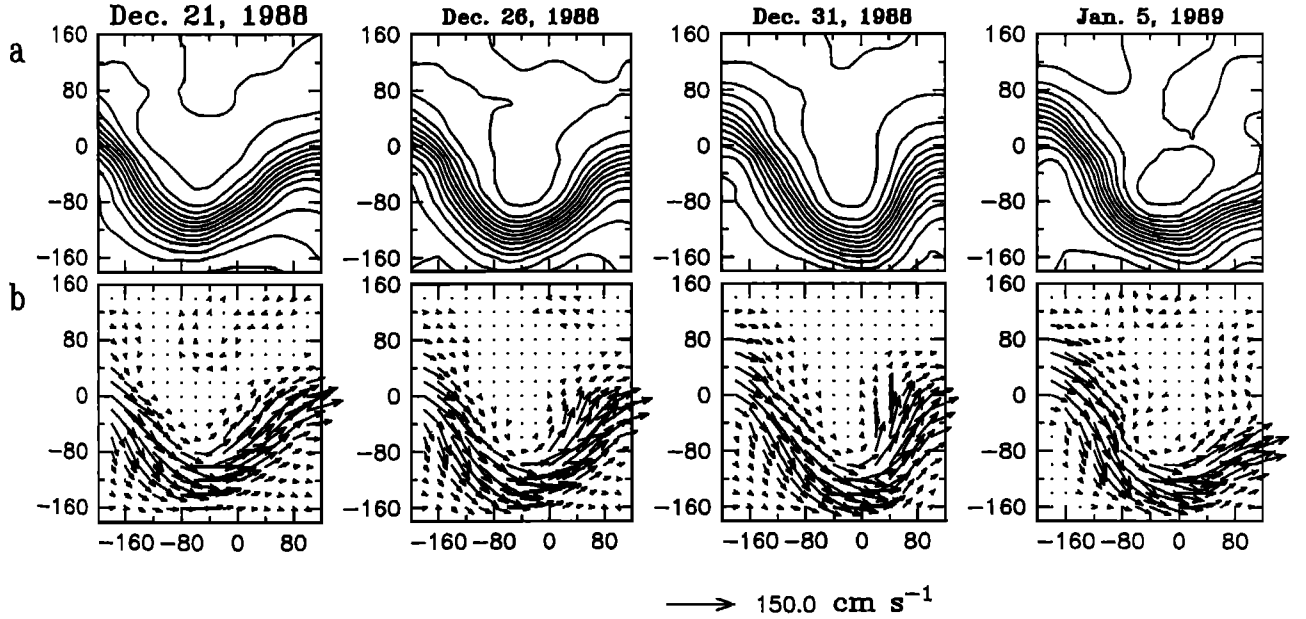

Figure 9. (a) Contoured optimal interpolation (OI) maps of $\Delta D_{400,1000}$ obtained in the SYNOP Central Array for the period December 21, 1988, to January 5, 1989. Each frame corresponds to the boxed region in Figure 8. Axes labels indicate horizontal distance in kilometers from the origin at 38°N, 68°W, where the x axis is oriented along 075°T. (b) The corresponding $\mathbf{V}_{\text{IES}}$ fields.

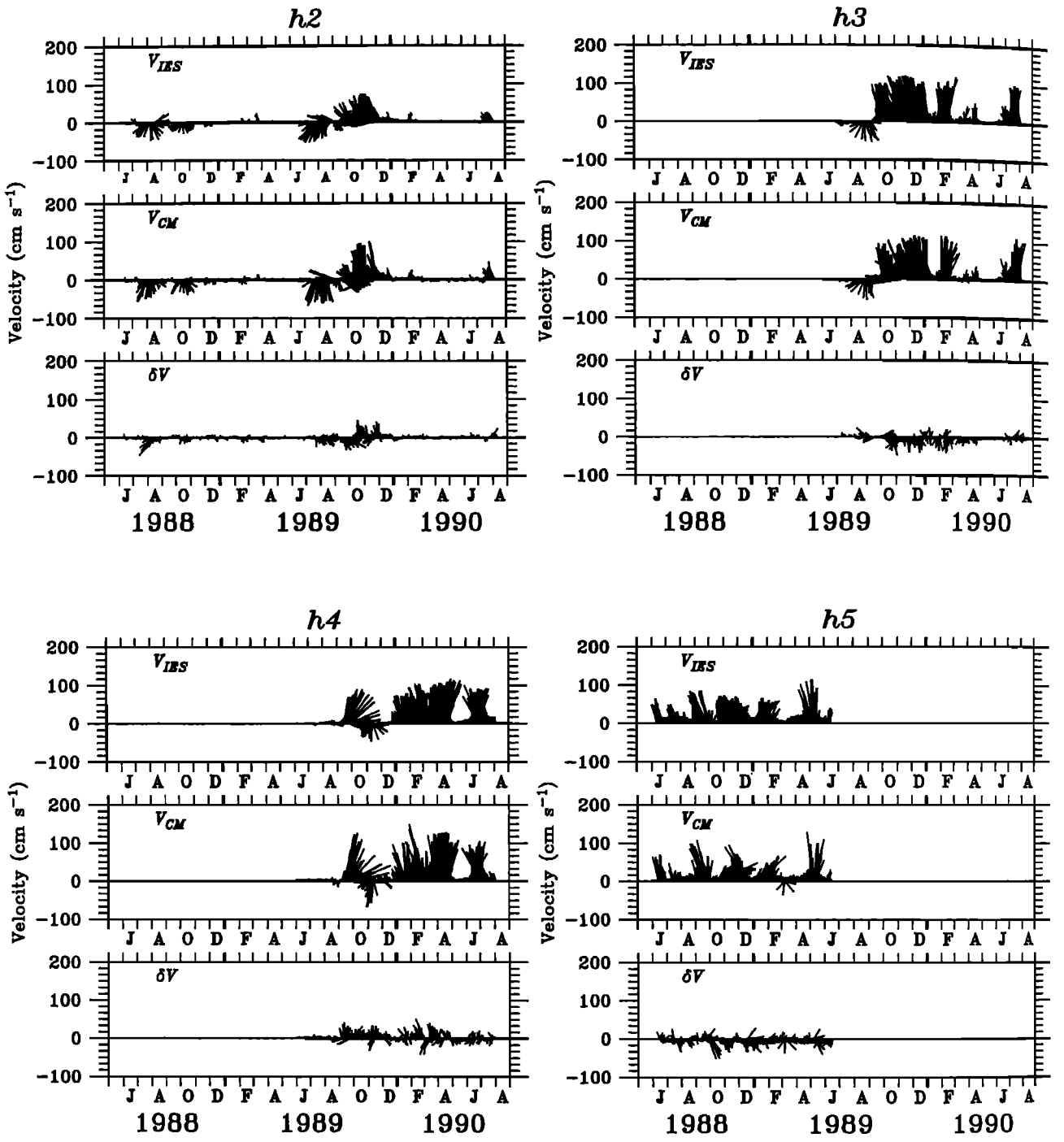

Figure 10. Top plot for each site showing the $\mathbf{V}_{IES}$ velocities calculated from the IES-derived $\Delta D_{400,1000}$ fields. Data for eight sites in the SYNOP Central Array are shown for the period May 1988 to August 1990. Middle plot for each site showing the shear velocities $\mathbf{V}_{CM}$ measured directly by current meters at 400 dbar relative to 1000 dbar. Bottom plot for each site showing the difference vectors $\delta\mathbf{V} = \mathbf{V}_{IES} - \mathbf{V}_{CM}$. Upward pointing vectors indicate eastward flow; the speed scale (cm s^{-1}) is as shown on the vertical axes.

near the bottom into the high-velocity Gulf Stream core. At three of the sites (h_2, h_3, and i_2), acoustic Doppler current profilers (ADCPs) were placed above the topmost current meters to monitor the velocity structure of the upper 400 m. The 100 and 200 m currents used in this paper were measured by the ADCPs. Current shears were obtained by differencing the observed currents at selected pairs of depths. Complete descriptions of the ADCP, IES, and CM data sets are given by *Johns et al.* [1995], *Watts et al.* [1995], and *Shay et al.* [1995].

3.3. Comparison of Velocity Shears

Fields of vector baroclinic velocity $\mathbf{V}_{IES}$ were estimated from the two-dimensional gradients of the OI maps of $\Delta D_{i,j}(\tau)$ using (7). Figure 9b shows the velocity fields corresponding to the $\Delta D_{400,1000}$ maps shown in Figure 9a.

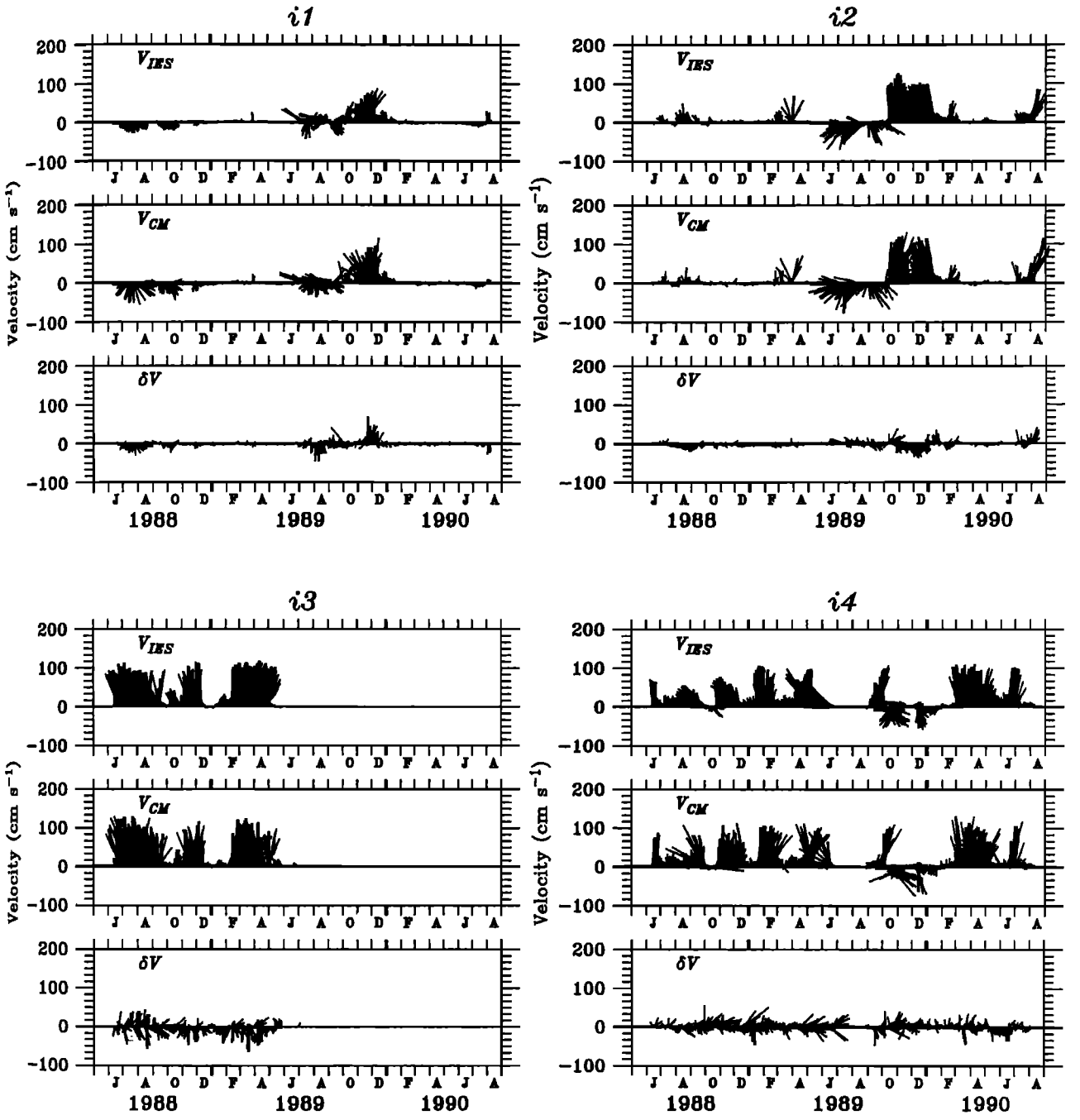

Figure 10. (continued)

The currents are small where the dynamic height gradients are weak and reach maximum speeds of 110–121 cm s^{-1} in the core of the Gulf Stream where the ΔD gradients are strongest.

Comparisons of these derived baroclinic velocities V_{IES} and the directly measured velocity shears V_{CM} were made at the individual mooring sites. The V_{IES} and V_{CM} are compared for the (400, 1000 dbar) range in Figure 10 for two lines of four moorings spanning from north to south across the Gulf Stream. (Four of these comparisons were limited to one observational year because of instrument failures.) There is excellent agreement between the two velocity estimates. With exceptions discussed below, the calculated velocities exhibit nearly the same speed and direction as the observed velocity shears. The plots of the residual vectors $\delta V = V_{IES} - V_{CM}$ (bottom plot for each site) show that typically, the differences are small. The agreement between these two velocity estimates can be quantified by examining Table 3, which lists the rms values of the u and v components for both V_{IES} and V_{CM} as well as for δV. Both V_{IES} and V_{CM} produce similar rms values for the two velocity components, indicating that the V_{IES} determined from the $\Delta D_{400,1000}$ maps accurately capture the observed variance.

For the most part, the δV vectors shown in Figure 10 do not exhibit bias. However, there are sites and time periods when the V_{IES} currents either underestimate or overes-

Table 3. Root-Mean-Square Variability of the Directly Measured and Derived Currents at 400 dbar Relative to 1000 dbar in the SYNOP Array are Listed for Each Component

		Root-Mean-Square					
		u component			v component		
Site	Mean Speed	u_{IES}	u_{CM}	δu	v_{IES}	v_{CM}	δv
			Middle Frontal Region				
h3	39.92	51.97	46.19	12.22	17.94	17.97	9.56
h4	35.48	46.31	50.10	12.29	19.24	18.92	7.64
i3	55.80	62.89	59.00	18.85	23.43	18.92	11.14
i4	37.51	43.00	34.73	12.57	22.97	22.44	14.96
			Northern Frontal Region				
h2	12.11	16.20	20.54	7.83	12.38	13.25	6.72
i1	11.49	15.91	19.04	8.54	12.13	14.22	6.48
i2	21.86	32.52	32.39	8.94	15.25	17.09	7.80
			Southern Frontal Region				
h5	33.59	37.13	32.70	12.74	18.48	17.02	12.19

The rms values of the difference vectors are also listed. Values given in cm s^{-1}. SYNOP, Synoptic Ocean Prediction.

timate the observed flow. For example, at site h_3, $\mathbf{V}_{IES}$ is generally smaller than $\mathbf{V}_{CM}$ during October 1989 to April 1990, but during July–August 1990 the calculated currents exceed the observations. By examining the daily OI maps it was found that such cases were often associated with events in which the path curvature was large. Typically, the observed currents were larger than $\mathbf{V}_{IES}$ currents when anticyclonic meander crests (negative curvature) were present, and the opposite situation occurred when meander troughs (positive curvature) were present. Recalling that the $\mathbf{V}_{IES}$ velocities are geostrophic estimates, the sense of these differences has been shown by gradient balance calculations [*Howden*, 1996] to be in accord with the respective supergeostrophic and subgeostrophic currents which occur in anticyclonic and cyclonic portions of jets [e.g., *Holton*, 1979].

Using the IES measurements, geostrophic velocities were also calculated for other pressure intervals. Estimates of $\mathbf{V}_{IES}$ were determined for 100, 200, 400, 700, and 1000 dbar relative to 3500 dbar. These levels were chosen to coincide with the depths of the current meter and ADCP measurements. Figure 11 presents the velocities determined from the IESs for site i_2 together with the observed velocity shears. The IES-derived velocities at 100, 200, and 400 dbar agree strikingly well with the directly measured currents in both speed and direction. At 700 dbar and even at 1000 dbar the agreement is good when the currents are strong. However, at the 700 and 1000 dbar levels, when the main baroclinic front meanders away from this current meter site, other small signals are evident in the current meter records which are not well represented by the geostrophic estimates from the IESs.

3.4. Sources of Error

Table 3 indicates that the minimum rms error is 6–8 cm s^{-1}. In general, the errors increase as the current speeds increase, where the additional u component error contribution is 15–20% of the current speed.

Table 4 summarizes several factors which have been identified as sources of these differences and summarizes the size of each factor's contribution. Error in the directly measured currents accounts for 0.02–0.04 m s^{-1} of the observed differences. This includes the actual measurement error as well as errors introduced by the mooring motion compensation procedure used to adjust the measurements to constant horizons [*Cronin and Watts*, 1996]. Another source of error is the OI procedure used to map the IES dynamic height measurements from the SYNOP grid designed for mapping the mesoscale. Using the OI error estimates and guided also by results from *Kim and Watts* [1994], errors in the ΔD gradients contribute 0.03–0.13 m s^{-1} to the geostrophic velocity differences (the size of this error depends mainly on current speed). A third source of error is attributed to the modeled $\Delta D_{i,j}(\tau)$ relationships, shown in Figure 2; they do not fit the observations at all pressure intervals equally well. Velocity errors of 0.04–0.09 m s^{-1} are attributed to these uncertainties. Finally, ageostrophic components of the flow account for the remaining, often the largest, errors. These components are measured by the current meters but are absent in the $\mathbf{V}_{IES}$ velocities. Mesoscale ageostrophic components, for which the largest terms increase with $|\mathbf{V}|^2$ and with path curvature, account for 0.04–0.25 m s^{-1} of the differences in the velocity estimates [*Johns et al.*, 1989; *Kontoyiannis and Watts*, 1990; *Kim*, 1991]. Submesoscale ageostrophic components account for 0.05–0.10 m s^{-1}.

Because the sizes of the $\delta\mathbf{V}$ vectors scale roughly with the magnitude of the current, three regimes are identified here, in which the various error sources make different contributions.

1. For weak currents (<30 cm s^{-1}) the differences are <10 cm s^{-1}. The observation that the differences between

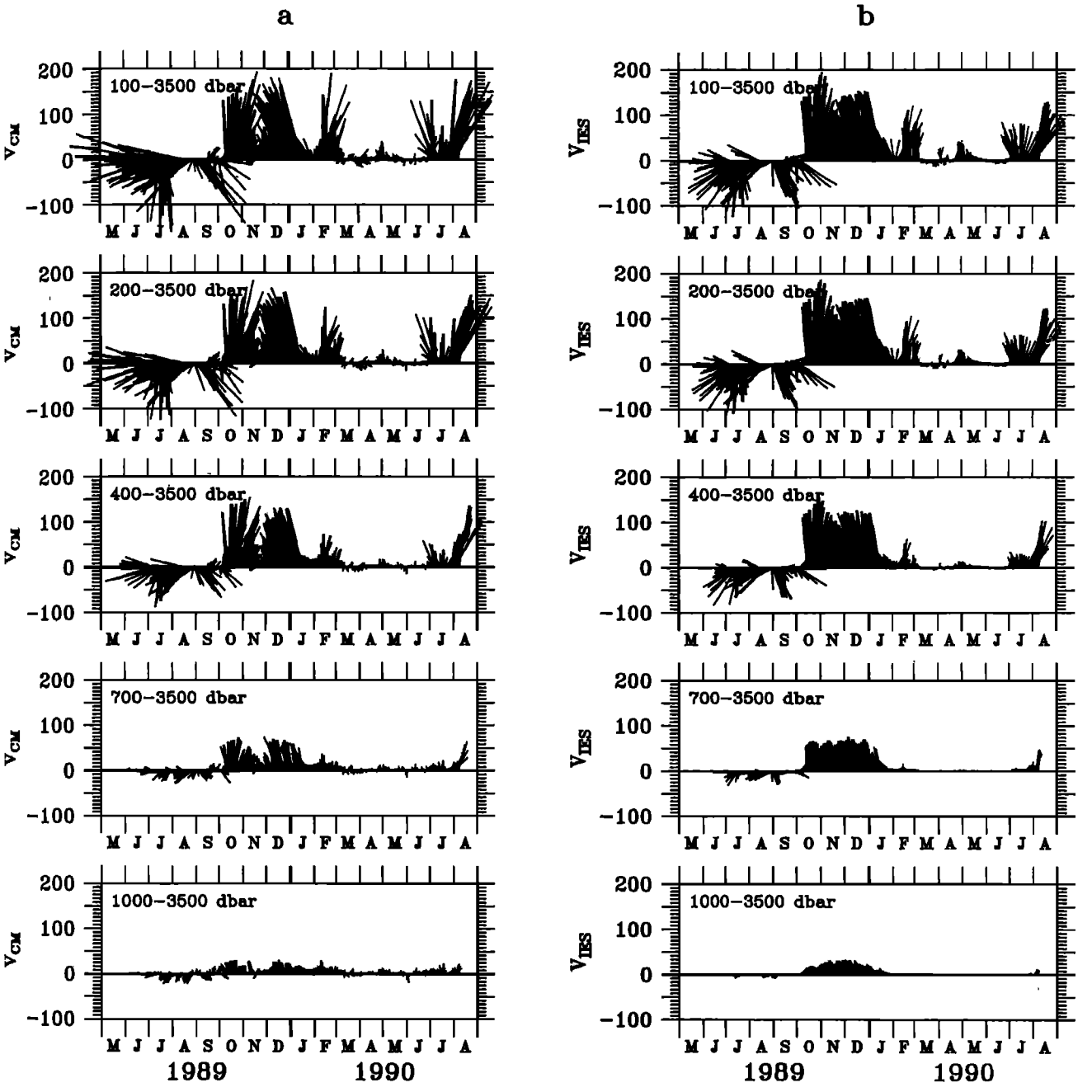

Figure 11. Currents at site i2 for the period May 1989 to August 1990. (a) V_{CM} are directly measured currents by ADCP at 100 and 200 dbar and by current meters at 400, 700, 1000, and 3500 dbar. (b) V_{IES} are currents computed from $\Delta D_{i,j}$ at the corresponding levels. All velocities are relative to the 3500 dbar level. Upward pointing vectors indicate eastward flow; the speed scale (cm s^{-1}) is as shown on the vertical axes.

V_{IES} and V_{CM} are small when the currents are weak indicates that several of the terms listed in Table 4 must also be small. In particular, errors associated with mooring motion compensation, mesoscale ageostrophic currents, and the measured $\nabla\tau$ all tend toward zero when the current is small. Therefore the minimum error level arises mainly from the presence of small-scale ageostrophic currents which are measured by the current meters but not the IESs.

2. For moderate currents (40–80 cm s^{-1}) the differences are 10–20 cm s^{-1}. Three roughly equal sources of error account for the differences observed. The small-scale ageostrophic currents still account for $\delta V \sim 6$–8 cm s^{-1}. However, two additional terms make nearly equal contributions to the differences (Table 4): errors associated with estimating $\nabla\tau$ from the IESs and uncertainties in $d[\Delta D_{i,j}(\tau)]/d\tau$. Each of these three terms accounts for errors that are ~10% of the observed currents in this range of current strengths.

3. For strong currents (> 90 cm s^{-1}) the differences are 20–30 cm s^{-1}. In this regime, all the source terms identified in Table 4 contribute to the observed differences. In particular, cyclostrophic accelerations grow with $|V|^2$. These

Table 4. Sources of Error in the Directly Measured and Geostrophically Derived Currents

Source Term	Relative error (%)	Contribution to δV (m s^{-1})	Reference
Errors in directly measured velocity			
Measurement error by CMs (mooring motion compensated)	4–8	0.02–0.04	Cronin *et al.* [1992]
Ageostrophic motions of small horizontal or vertical-scale	10–20	0.05–0.10	Johns and Zantopp [1991]
Mesoscale ageostrophic motions	7–25	0.04–0.25	Johns *et al* [1989], Kontoyiannis and Watts [1990], Kim [1991], and Howden [1996]
Subtotal	13–33	0.07–0.27	
Errors in geostrophic velocity			
Errors in $d[\Delta D_{i,j}(\tau)]/d\tau$	8–10	0.04–0.09	this work
Errors in measured τ and in $\nabla\tau$	7–15	0.03–0.13	this work and Kim and Watts [1994]
Subtotal	11–18	0.05–0.16	

Total error depends on current strength; see section 3.4 regarding weak, moderate, and strong currents.

mesoscale ageostrophic effects can cause the currents to differ from geostrophic balance by more than the other error sources combined.

4. Discussion and Summary

This work has investigated the relationship between the dynamic height anomaly $\Delta D_{i,j}$ and the IES-measured travel time τ over a variety of pressure intervals (p_i,p_j). In regions with strong baroclinic fronts the variations in τ and $\Delta D_{i,j}$ observed at any given site are caused primarily by changes in thermocline depth as the front shifts laterally over the site. Using historical hydrographic data from the Gulf Stream, a formulation for $\Delta D_{i,j}(\tau)$ has been developed which is more general than the linear function defined by *Rossby* [1969] and *Watts and Rossby* [1977].

A four-parameter parallel isotherms model was used to represent the functional dependence of $\Delta D_{i,j}(\tau)$ on pressure limits that span at least some portion of the main thermocline. The relatively small NSRs (~1%) in Table 2 verify that the relationship $\Delta D_{i,j}(\tau)$ in the Gulf Stream region is well defined. These functional relationships provide a method for calculating the baroclinic geostrophic velocity profile from the τ measurements of neighboring pairs of IESs; two-dimensional arrays of instruments can resolve both components of velocity.

The fact responsible for the existence of the suite of dynamic height curves (Figure 2) is that the variability of the Gulf Stream and the neighboring eddy field is dominated by the lowest baroclinic mode, or gravest empirical mode (GEM). This is readily apparent by examining Figure 12, which shows very high (exceeding the 99% confidence level) vertical correlations for velocity and temperature records in the main thermocline region. These data come from year-long current meter and ADCP records in the Central Array (at sites h3, h4, and i2 in Figure 8). The records used for this calculation were not corrected for mooring motion, and even higher correlations were obtained when the motion-corrected records were used. Temperature records are extremely highly correlated from the thermocline to the 3500 m level. However, the 3500 m velocities are not correlated with the upper levels, implying that either vertical phase offsets are $O(\pi/2)$ in the stream functions or other bottom-

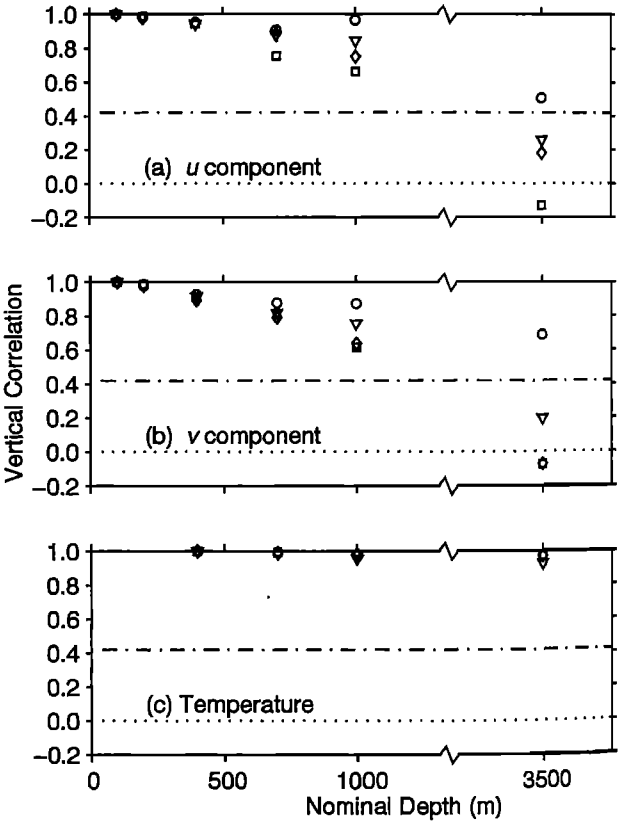

Figure 12. (a) and (b) Vertical correlations of the 100 m velocity with velocity measured at nominal depths of 100, 200, 400, 700, 1000, and 3500 m. (c) Temperature correlations with the 400 m temperatures, since no T measurements were obtained above 400 m. Circles, squares, triangles, and diamonds designate moorings: h4–1989, h3–1989, i2–1990, and h3–1990, respectively. The dashed-dotted line indicates the 99% confidence level. The zero line is dotted.

intensified motions (such as topographic Rossby waves) are important in the deep ocean in this region.

It is essential to realize that the GEM represents a more general concept than flat-bottom dynamical modes that are keyed to just one particular assumed basic stratification $N^2(z)$. *Pickart and Watts* [1990] did apply a dynamical modes technique to IES data under the Gulf Stream at Cape Hatteras, but they noted that the method would only be effective where the amplitude of meandering was small. In other regions the thermocline or pycnocline depth can exhibit great changes, both spatially and temporally, in mesoscale variability. Observations show that lateral variations in density, dynamic height, and velocity shear all shift vertically as the pycnocline changes depth. The remarkably high vertical correlations of velocity and temperature that were shown in Figure 12 attest to the relative low variance of higher-order vertical structure. As a result, the observed variability may be approximated by the parallel isotherms model (section 2.3), and the resulting velocity profiles represent the data much more accurately than dynamical modes.

The geostrophic velocities obtained in this manner were compared with shear velocities measured by current meters. Overall, there is good agreement between the two estimates, both in current strength and direction. The differences depend upon current speed, as summarized at the end of section 3.4, and can be attributed mainly to small-scale and mesoscale ageostrophic circulations which are only measured by the current meters. Curvature-related ageostrophic components account for the largest differences. The errors in geostrophic velocity shear determined from dynamic height ($\Delta D_{400,1000}$) gradients mapped by the IESs were 12 cm s^{-1} in the presence of typical currents of 50 cm s^{-1}.

The main point of this new study is that the vertical structure of the dynamic height field can be determined for a suite of depth ranges from the single measurement of τ. Furthermore, by knowing the dynamic height profile at neighboring IES sites the vertical structure of geostrophic currents can be accurately determined. The appearance of getting more than one piece of information from the single measurement of τ arises from having done the above inversion of historical hydrographic data, by fitting it to the parallel isotherms model structure of $\Delta D_{i,j}(\tau)$. Vital to the success of this technique is the availability of high-quality, full water column historical hydrocasts in the region of interest. By examining a representative set of hydrographic measurements, not only is it possible to determine the $\Delta D_{i,j}(\tau)$ relationships, but it is also possible to predict the error levels a priori, and hence to judge whether this technique is appropriate for a new region. Work is currently underway to apply the GEM concept, without the parallel isotherms restriction, to the Newfoundland Basin and Subantarctic Front regions.

Acknowledgments. We are grateful to Bill Johns for providing the ADCP data and to Mike McCartney for the quality-controlled set of bottle stations. We would also like to thank one of the reviewers for suggesting Figures 5a and 6. This work was supported by the Office of Naval Research and the National Science Foundation.

References

Chaplin, G., and D. R. Watts, Inverted echo sounder development, *IEEE Ocean '84 Conf. Rec., 1*, pp. 249–253, Int. of Electr. and Electr. Eng., New York, 1984.

Chiswell, S. M., D. R. Watts, and M. Wimbush, Using inverted echo sounders to measure dynamic height in the eastern equatorial Pacific during the 1982–83 El Niño, *Deep Sea Res., Part A, 34*, 981–991, 1986.

Chiswell, S. M., D. R. Watts, and M. Wimbush, Inverted echo sounders observations of variability in the eastern equatorial Pacific during the 1982–83 El Niño, *Deep Sea Res., Part A, 34*, 313–327, 1987.

Chiswell, S. M., M. Wimbush, and R. Lukas, Comparison of dynamic height measurements from an inverted echo sounder and an island tide gauge in the central Pacific, *J. Geophys. Res., 93*, 2277–2283, 1988.

Cronin, M., and D. R. Watts, Eddy-mean flow interaction in the Gulf Stream at 68°W, I, Eddy energetics, *J. Phys. Oceanogr., 26*, 2107–2131, 1996.

Cronin, M., K. L. Tracey, and D. R. Watts, Mooring motion correction of SYNOP Central Array current meter data, *Tech. Rep. 92–4*, 114 pp., Grad. Sch. of Oceanogr., Univ. of R. I., Narragansett, 1992.

Garzoli, S. L., and Z. Garraffo, Transports, frontal motions, and eddies at the Brazil-Malvinas Currents Confluence, *Deep Sea Res., Part A, 36*, 681–702, 1989.

Garzoli, S. L., and A. L. Gordon, Origins and variability of the Benguela Current, *J. Geophys. Res., 101*, 897–906, 1996.

Hallock, Z. R., Regional characteristics for interpreting inverted echo sounder (IES) observations, *J. Atmos. Oceanic Technol., 4*, 298–304, 1987.

Holton, J. R., *An Introduction to Dynamic Meteorology*, Academic Press, San Diego, Calif., 1979.

Howden, S. D., Processes associated with steep meander development in the Gulf Stream near 68°W, Ph.D. dissertation, 229 pp., Grad. Sch. of Oceanogr., Univ. of R. I., Narragansett, 1996.

Johns, E., D. R. Watts, and H. T. Rossby, A test of geostrophy in the Gulf Stream, *J. Geophys. Res., 94*, 3211–3222, 1989.

Johns, W. E., and R. J. Zantopp, The SYNOP experiment: Moored acoustic doppler current profiler data for the period June 1988 to August 1990, *Tech. Rep. 91–003*, 130 pp., Rosenstiel Sch. Mar. Atmos. Sci., Univ. of Miami, Miami, Fla., 1991.

Johns, W. E., T. J. Shay, D. R. Watts, and J. M. Bane, Gulf Stream structure, transport, and recirculation at 68°W, *J. Geophys. Res., 100*, 817–838, 1995.

Katz, E. J., Seasonal response of the sea surface to the wind in the equatorial Atlantic, *J. Geophys. Res., 92*, 1885–1893, 1987.

Kim, H.-S., An observational streamfunction in the Gulf Stream, M.S. thesis, 109 pp.,Grad. Sch. of Oceanogr., Univ. of R. I., Narragansett, 1991.

Kim, H.-S., and D. R. Watts, An observational streamfunction in the Gulf Stream, *J. Phys. Oceanogr., 24*, 2639–2657, 1994.

Kontoyiannis, H., and D. R. Watts, Ageostrophy and pressure work in the Gulf Stream at 73°, *J. Geophys. Res., 95*, 22209–22228, 1990.

Miller, L. L., D. R. Watts, and M. Wimbush, Oscillation of dynamic topography in the eastern equatorial Pacific, *J. Phys. Oceanogr., 15*, 1759–1770, 1985.

Pickart, R. S., and D. R. Watts, Using the inverted echo sounder to measure vertical profiles of Gulf Stream temperature and geostrophic velocity, *J. Atmos. Oceanic Technol., 7*, 146–156, 1990.

Rossby, H. T., On monitoring depth variations of the main thermocline accoustically, *J. Geophys. Res., 74*, 5542–5546, 1969.

Shay, T. J., J. M. Bane, D. R. Watts, and K. L. Tracey, Gulf Stream flow field and events near 68°W, *J. Geophys. Res., 100*, 22565–22589, 1995.

Tracey, K. L., S. D. Howden, and D. R. Watts, IES calibration and mapping procedures, *J. Atmos. Oceanic Technol., 14*, 1483–1493, 1997.

Trivers, G. A., and M. Wimbush, Using acoustic travel time to determine dynamic height variations in the North Atlantic Ocean, *J. Atmos. Oceanic Technol., 11*, 1309–1316, 1994.

Watts, D. R., and H. T. Rossby, Measuring dynamic heights with inverted echo sounders: Results from MODE, *J. Phys. Oceanogr., 7*, 345–358, 1977.

Watts, D. R., K. L. Tracey, J. M. Bane, and T. J. Shay, Gulf Stream path and thermocline structure near 74°W and 68°W, *J. Geophys. Res., 100*, 18291–18312, 1995.

Wimbush, M., S. M. Chiswell, R. Lukas, and K. A. Donohue, Inverted echo sounder measurement of dynamic height through an ENSO cycle in the central equatorial Pacific, *IEEE J. Oceanic Eng., 15*, 380–383, 1990.

Y. He, K. L. Tracey, and D. R. Watts, University of Rhode Island, Graduate School of Oceanography, Narragansett Bay Campus, Narragansett, RI 02882. (e-mail: yhe@canr1.cag.uconn.edu; karen@calvin.gso.uri.edu; randy@drw.gso.uri.edu)

(Received January 17, 1997; revised August 12, 1997; accepted November 3, 1997.)